ARTICLE OPEN

Check for updates

Morphology simulation of drop-on-demand inkjet-printed droplets

Shaowei Hu[1,2], Wenbo Zhu[1,2], Wanchun Yang[1] and Mingyu Li[1]✉

Inkjet-printed electronics have become a popular research topic in recent years. For common drop-on-demand (DOD) inkjet printing technology, uneven edges are a universal problem. Many factors, such as the properties of the ink and printing parameters, influence this problem, and numerical methods are better than experimental methods for studying these influences. In this paper, a model based on the Volume of Fluid (VOF) method and user-defined files (UDFs) in Ansys F is established to simulate the formation process of deposited ink droplets. The model and UDFs include the friction effect, and the morphology of a single droplet, two fused droplets, and multiple droplets is simulated to study the influence of different factors; some results can serve as guidelines for improving pattern quality. Finally, the effect of selective treatment is also studied to understand its advantages for inkjet printing.

npj Flexible Electronics (2022)6:64 ; https://doi.org/10.1038/s41528-022-00187-3

INTRODUCTION

With the development of science and technology, flexibility and wearability have become important characteristics for electronic products[1–3], such as flexible displays[4,5], solar cells[6,7], RFID systems[8–10], and wearable health-care sensors[11–13]. Printing technologies for printing electronics, such as screen printing[14,15], inkjet printing[16,17], and transfer printing[18–20], have been developed and studied extensively because of their low cost and large areas[21]. Inkjet printing, as a mature digital controlled technology, has features of noncontact printing[22] and pattern designability[23] and is widely used for the printing of conductive[24–26], semiconductive[27,28] and dielectric[29,30] materials. In inkjet printing technologies, continuous inkjets always waste ink[31], and advanced inkjet printers such as those with aerosol jets[32] and electrohydrodynamic jets[33] are specialized for small-scale refined patterns. Considering the printing scale, efficiency, and cost, a conventional drop-on-demand (DOD) inkjet printer is very suitable for printed electronics[34]. However, there are also several problems associated with fabricating patterns by a DOD inkjet. Individual droplets cannot be exactly arranged along the bevel outlines, and uneven edges will cause anisotropic patterns and other potential problems[35]. There is also a conflict between printability and pattern resolution; a relatively low contact angle improves the printability of the ink, but an increased droplet area affects the pattern resolution[36,37].

The problems mentioned above have limited the wide usage of inkjet printing electronics. Moreover, the physical properties of the ink such as viscosity and surface tension also influence the formation of patterns[38]. Many types of solvent may be considered for a given functional material, and solvent selection is an important issue. To solve the above problems, the morphology formation rules of droplets should be studied systematically, and numerical simulation is a suitable method to research this subject.

Numerical simulations of inkjet technologies have been conducted by several researchers. Stringer and Derby studied the deposition and formation of multiple droplets by theoretical analysis of experimental data, and they found that there are maximum and minimum values of drop spacing to allow printing of stable lines[39], but they did not change the solvent or printing frequency. Lee et al. numerically investigated droplet impingement and coalescence dynamics using the sharp-interface level-set method[40] and illustrated that advancing and receding contact angles play important roles in this process. Zhang et al. simulated the morphology of a line of multiple deposited droplets with a lattice Boltzmann model[41], they obtained all types of printed lines but did not study the influence of printing frequency. From existing studies, both properties of ink (impact velocity, surface tension, viscosity) and printing parameters (drop spacing) have an influence on printed patterns, but these studies always only study part of the factors in the printing process, an overview of this question is still not clear. Therefore we try to systematically research the influence of properties of ink and printing parameters in this study and gave several guidelines for fabricating inkjet-printed electronics.

A suitable model is necessary to achieve reliable simulated results. Numerical studies of one droplet or multiple droplets impacting a solid surface have been conducted by many researchers[42–45]. In these studies, the VOF method is the most popular multiphase model, as it is a convenient way to define the initial state of droplets and construct interfaces[46]. The fundamental VOF method uses the static contact angle for boundary conditions; however, because of the friction between the fluid and the solid surface, the contact angle is not a single value in the real world[47]. The maximum value of the quasi-static contact angle is the advancing contact angle (θ_{adv}), the minimum value is the receding contact angle (θ_{rec}), and the difference between θ_{adv} and θ_{rec} is the contact angle hysteresis (CAH)[48]. These parameters obviously influence the morphology of tiny droplets and should be considered in the simulation model.

With the help of user-defined files (UDFs), researchers can apply variable contact angles as boundary conditions. In previous studies, the most promising formula for the dynamic contact

[1]Sauvage Laboratory for Smart Materials, School of Materials Science and Engineering, Harbin Institute of Technology (Shenzhen), 518055 Shenzhen, China. [2]These authors contributed equally: Shaowei Hu, Wenbo Zhu. ✉email: myli@hit.edu.cn

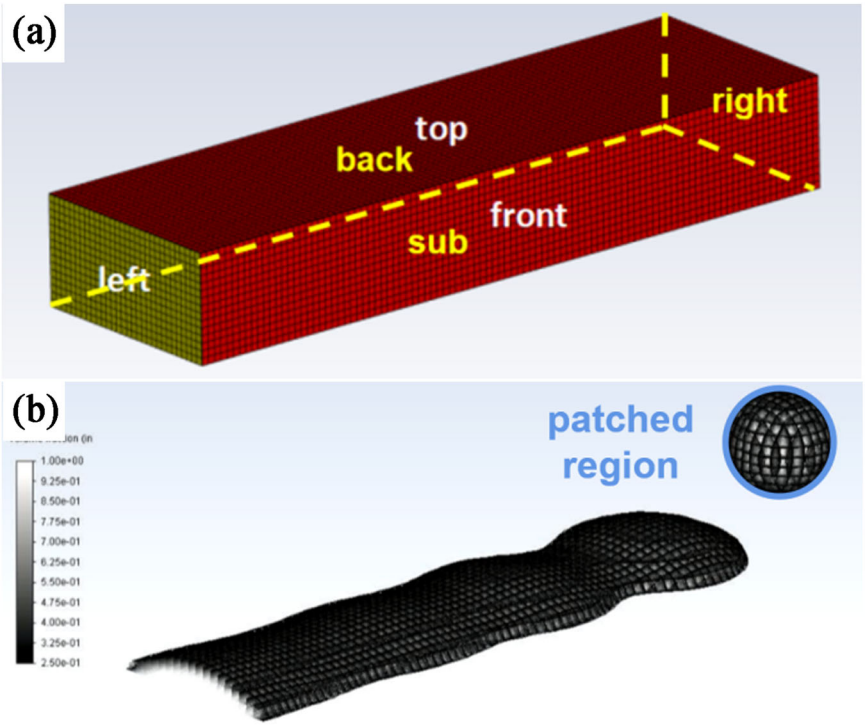

Fig. 1 Overview of the model. a Geometry of computational domain and meshes. **b** Deposited droplets and definition of the spherical droplet. **a** Is an overview of the computational domain and meshes drawn from ICEM, it is a cuboid divided by hexahedral meshes, and every mesh has dimensions on the 1 μm × 1 μm × 1 μm scale. Every side of the cuboid is named respectively in order to be defined as different types of boundaries in Fluent. **b** Is drawn from Fluent, which shows the deposited droplets and newly defined droplet region on air with an initial velocity.

Table 1. Parameters of ink droplet set in simulation.

Density	Viscosity	Surface tension	Contact angle	Impact velocity	Radius of roplet
800–1600 g m^{-3}	0.01–0.02 pa s	0.02–0.06 n m^{-1}	20–50°	4–12 m s^{-1}	10–20 μm

angle was the Hoffman function, which is summarized by Kilster[49] from Hoffman's experiments[50] as follows:

$$f_{\mathrm{Hoff}}(x) = \arccos\left\{1 - 2\tanh\left[5.16\left(\frac{x}{1+1.31x^{0.99}}\right)^{0.706}\right]\right\}$$
$$\theta_d = f_{\mathrm{Hoff}}\left[\mathrm{Ca} + f_{\mathrm{Hoff}}^{-1}(\theta_s)\right] \quad (1)$$

where θ_d is the dynamic contact angle, θ_s is the static contact angle and Ca is the capillary number, which is a dimensionless number equal to $v_{\mathrm{contline}} \cdot \eta/\gamma$[49]. In many studies, the Hoffman function is used in UDFs to calculate θ_d, which is then used as a boundary condition[51]. θ_d is calculated from the empirical equation based on the observed results; however, the contact angle set by the boundary condition in the simulation is similar to an interaction parameter between a fluid and a solid surface. A rational model should yield results that are consistent with experimental data; thus, the Hoffman function should be a criterion rather than a boundary condition.

For the reasons above, this paper establishes a model for morphology simulation of droplets that uses CAH UDFs based on force analysis at the contact line and discusses the rationality of models with CAH UDFs, with Hoff UDFs, or without UDFs. Then, single droplets and multiple droplets are simulated to study the influence of different factors, and finally, some principles to improve printing quality are proposed.

RESULTS AND DISCUSSION

Overview of the model

Geometry and meshes are built by ICEM software. As Fig. 1a shows, the computational domain is a cuboid divided by hexahedral meshes, and every mesh has dimensions on the 1 μm × 1 μm × 1 μm scale.

Multiphase is described by the VOF method, which defines the volume fraction (color function) of one of the fluids in each cell. The following conservation equations are solved in the computational domain:

$$\partial(\rho\mathbf{u})/\partial t + \nabla\cdot(\rho\mathbf{u}\times\mathbf{u}) = -\nabla p + \nabla\cdot(2\mu\mathbf{D}) + \mathbf{F}_{\mathrm{st}} + \rho\mathbf{g}$$
$$\partial\rho/\partial t + \nabla\cdot(\rho\mathbf{u}) = 0 \quad (2)$$

where ρ is density, $\mathbf{u}$ is velocity vector, t is time, p is pressure, μ is dynamic viscosity, $\mathbf{D}$ is the rate of deformation, $\mathbf{F}_{\mathrm{st}}$ is body force and $\mathbf{g}$ is gravity[46].

In this study, the first phase is air, and the second phase is ink. The viscosity type is laminar. Gravitational acceleration is -9.81 m s^{-2} along the z direction. Parameters of ink droplets are set as Table 1 shows, which are in accord with the real conditions.

The droplets are generated by patching a spherical region filled with a second phase and an initial velocity along the z direction, as shown in Fig. 1b. The patched regions determine the drop spacing,

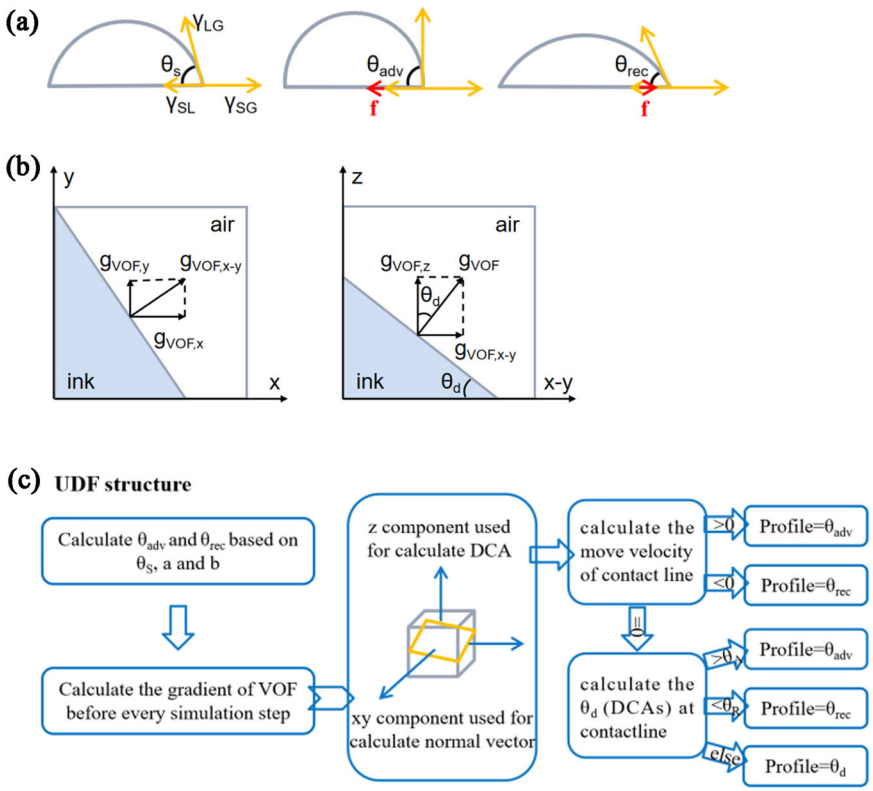

Fig. 2 Friction effect and designation of UDF. a Schematic diagram of friction tension and contact angle hysteresis. **b** The gradient of the VOF function from different views. **c** Structure of the CAH UDF. **a** Shows the relationship between friction effect and contact angle hysteresis, the red arrows represent the friction tension. **b** Shows the VOF gradients on the surface of ink fluid, the left figure is the vertical view and the right figure is lateral view.

and the interval time between droplets determines the printing frequency.

Friction effect and UDF

The CAH can be explained by the friction effect from Wang's study[52]. As Fig. 2a shows, a friction tension term f is added to Young's equation, and the value is positive if f and γ_{SL} have the same direction. It is assumed that the maximum value of f is f_{max} and $f \in [-f_{max}, f_{max}]$, similar to the static friction force. Some relations can be obtained as follows:

$$\begin{aligned} \gamma_{SG} &= \gamma_{LG}\cos\theta_s + \gamma_{SL} \\ \gamma_{SG} &= \gamma_{LG}\cos\theta_{adv} + \gamma_{SL} + f_{max} \\ \gamma_{SG} &= \gamma_{LG}\cos\theta_{rec} + \gamma_{SL} - f_{max} \end{aligned} \tag{3}$$

It can be concluded that $\cos\theta_s$ is the average of $\cos\theta_{adv}$ and $\cos\theta_{rec}$, and experimental data also support this relation[52,53]. However, this relation is not enough to conform to a certain value of $\cos\theta_{adv}$ and $\cos\theta_{rec}$.

Combining the experimental data and Cheng's theoretical analysis[54], it is assumed that for the contact angle of ink droplets (20–50°), CAH is linearly related to θ_s:

$$\begin{aligned} \mathrm{CAH} &= \theta_{adv} - \theta_{rec} = a\theta_s + b \\ 2\cos\theta_s &= \cos\theta_{adv} + \cos\theta_{rec} \end{aligned} \tag{4}$$

The kinetic friction force is similar to the maximum static friction force; similarly, the friction effect is f_{max} for a contact line moving forward and $-f_{max}$ for a contact line moving backward.

First, θ_{adv} and θ_{rec} are calculated. Then, the following formula is defined:

$$f(x) = \arccos(\cos\theta_s - x) - \arccos(\cos\theta_s + x) - a\theta_s - b \tag{5}$$

In this study, a is 0.5, and b is −5 (in degrees), based on the experimental data of the Ra0.1 surface[53]. The zero of this formula, x_0, can be found by the bisection method, and the UDFs θ_{adv} and θ_{rec} are defined as follows:

$$\begin{aligned} \theta_{adv} &= \arccos(\cos\theta_s - x_0) \\ \theta_{rec} &= \arccos(\cos\theta_s + x_0) \end{aligned} \tag{6}$$

Second, the moving direction (forward or back) of the contact lines and θ_d is defined. The VOF function gradient (g_{VOF}) of every cell in the computational domain is necessary to derive the parameters. Here, we use mature code to obtain the g_{VOF} values of three coordinate directions ($g_{VOF,x}$, $g_{VOF,y}$, and $g_{VOF,z}$)[55]. Then, some parameters are defined:

$$\begin{aligned} \mathrm{UDMI}_0 &= g_{VOF,x}/\sqrt{g_{VOF,x}^2 + g_{VOF,y}^2} \\ \mathrm{UDMI}_1 &= g_{VOF,y}/\sqrt{g_{VOF,x}^2 + g_{VOF,y}^2} \\ \mathrm{UDMI}_2 &= g_{VOF,z}/\sqrt{g_{VOF,x}^2 + g_{VOF,y}^2 + g_{VOF,z}^2} \end{aligned} \tag{7}$$

UDMI_i are user-defined parameters that can be saved and read in user-defined memory spaces for every cell, which are renewed in every calculation time step. Here, only cells at the interface of air and ink have useful UDMI_i values. As Fig. 2b shows, g_{VOF} is perpendicular to the interface, the contact line moves only along the x–y plane, and the unit normal vector of the contact line is

$$\mathbf{n}_{contline} = (\mathrm{UDMI}_0, \mathrm{UDMI}_1) \tag{8}$$

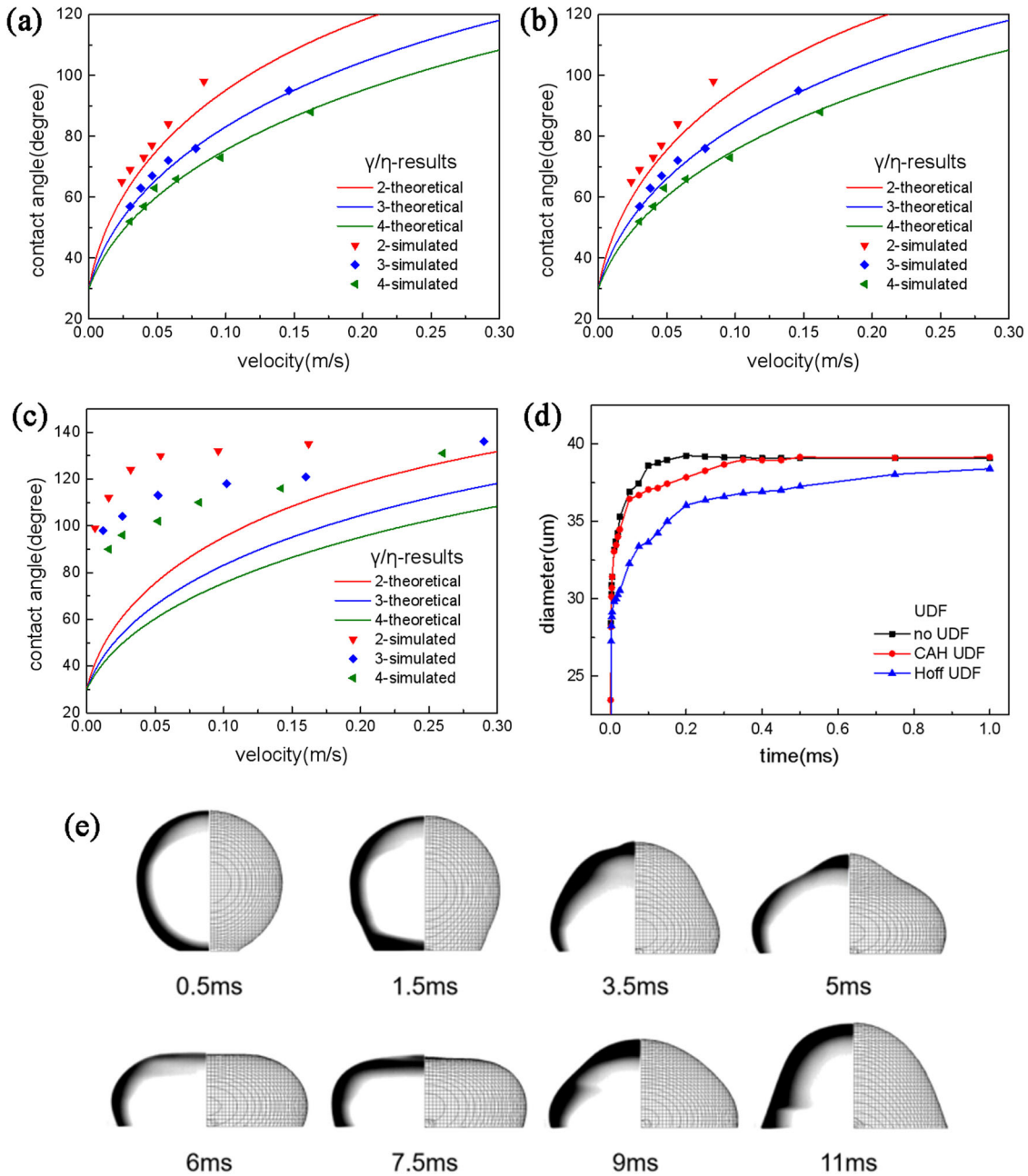

Fig. 3 Results of single droplet impact simulation. a Simulated results of cases without UDFs. **b** Simulated results of cases with the CAH UDF. **c** Simulated results of cases with the Hoff UDF. **d** Simulated time-dependent diameter of different cases. **e** Comparison of the simulated droplet and real droplet in ref. [56]. **a**–**c** Shows the relationship between derived simulated dynamic contact angle and moving velocity of the contact line. These figures show that results from cases without UDFs and cases with CAH UDF are in accord with the Hoffman function. In **e**, every picture is composed of photographs from ref. [56] (left part) and simulated shape from the case with CAH UDF (right part).

In FLUENT, the velocity of a fluid phase (ink) **v** can be directly read, and its velocity along the normal direction is

$$v_{\text{contline}} = \mathbf{v} \cdot \mathbf{n}_{\text{contline}} = v_x \text{UDMI}_0 + v_y \text{UDMI}_1 \tag{9}$$

If $v_{\text{contline}} > 0$, this piece of contact line moves forward, and if $v_{\text{contline}} < 0$, the contact line moves backward. Then, the dynamic contact angle θ_d is calculated by

$$\theta_d = \arccos(\text{UDMI}_2) \tag{10}$$

The forces at the contact line are directly reflected in quasi-static cases, as discussed. As a result, for contact lines moving forward, the boundary condition is θ_{adv}, and for contact lines moving backward, the boundary condition is θ_{rec}. If the contact line is not moving but it may move, θ_d is needed. When $\theta_d > \theta_{adv}$, the contact line should move forward, and the boundary condition is θ_{adv}. Similarly, if $\theta_d < \theta_{rec}$, the boundary condition is θ_{rec}. If $\theta_{rec} \le \theta_d \le \theta_{adv}$, the force at the contact line is wetted and maintains its quasi-static state, and the boundary condition is θ_d. The frame of the UDF is shown in Fig. 2c, and the UDF works on every cell and is renewed every time step.

Single droplet impact simulation

To compare the agreement between the Hoffman function of different models and experimental data, θ_d and v_{contline} should be

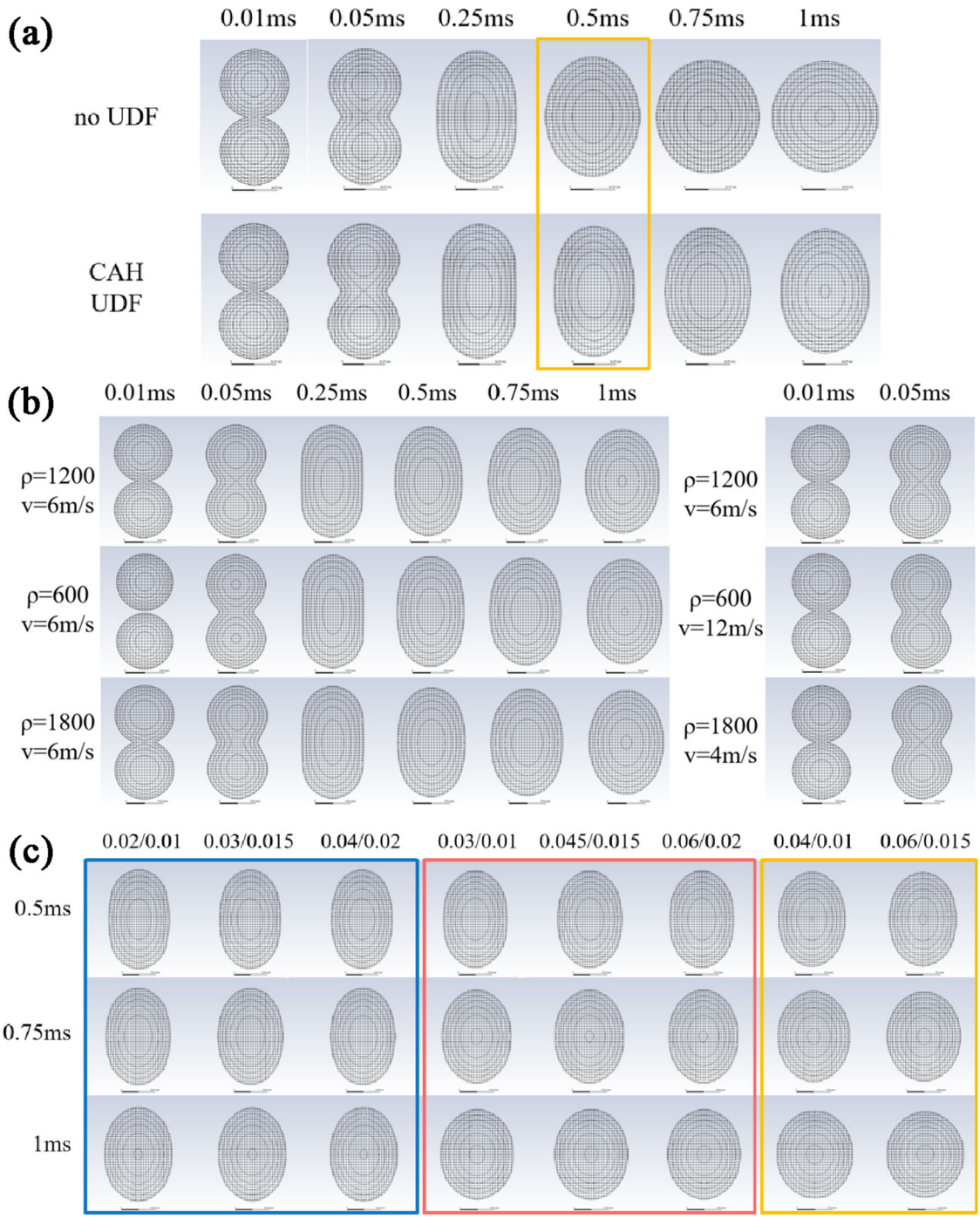

Fig. 4 Results of two droplets fusion simulation. a Simulated two-droplet fusion morphology of cases without a UDF and with the CAH UDF. **b** Simulated two-droplet fusion morphology of cases with different densities and impact velocities. **c** Simulated two-droplet fusion morphology of cases with different surface tensions and viscosities. All pictures are top views of simulated two-droplet fusion morphology. **a** Shows the difference between cases without UDFs and with CAH UDF. **b** Results reveal that the influence of impact velocity and density mainly worked in the early stage(<0.05 s) and can be ignored in the whole printing process. **c** Shows that the same value of surface tension/viscosity is the major factor that determines the simulated morphology at different times.

derived from simulation results. θ_d is directly estimated from the profile image, and $v_{contline}$ is calculated as $UDMI_i$ and read from the results. In addition to $v_{contline}$, the ratio of surface tension and viscosity γ/η determines the capillary number Ca. The simulated results and curves of the Hoffman function with different γ/η and $\theta_s = 30°$ values are shown in Fig. 3a–c. For cases without UDFs and with the CAH UDF presented in this study, the simulated points are in good agreement with the curves of the Hoffman function. In contrast, for cases with the Hoff UDF, the simulated points have a higher θ_d than the theoretical value. These results indicate that the basic VOF method in FLUENT is able to reproduce the Hoffman function. For cases with the CAH UDF, the applied boundary condition is not too different from 30° to cause obvious differences when Ca is dominant. For cases with Hoff UDF, the applied boundary condition is much higher than 30°, so the simulated points have much higher θ_d values. Figure 4d shows

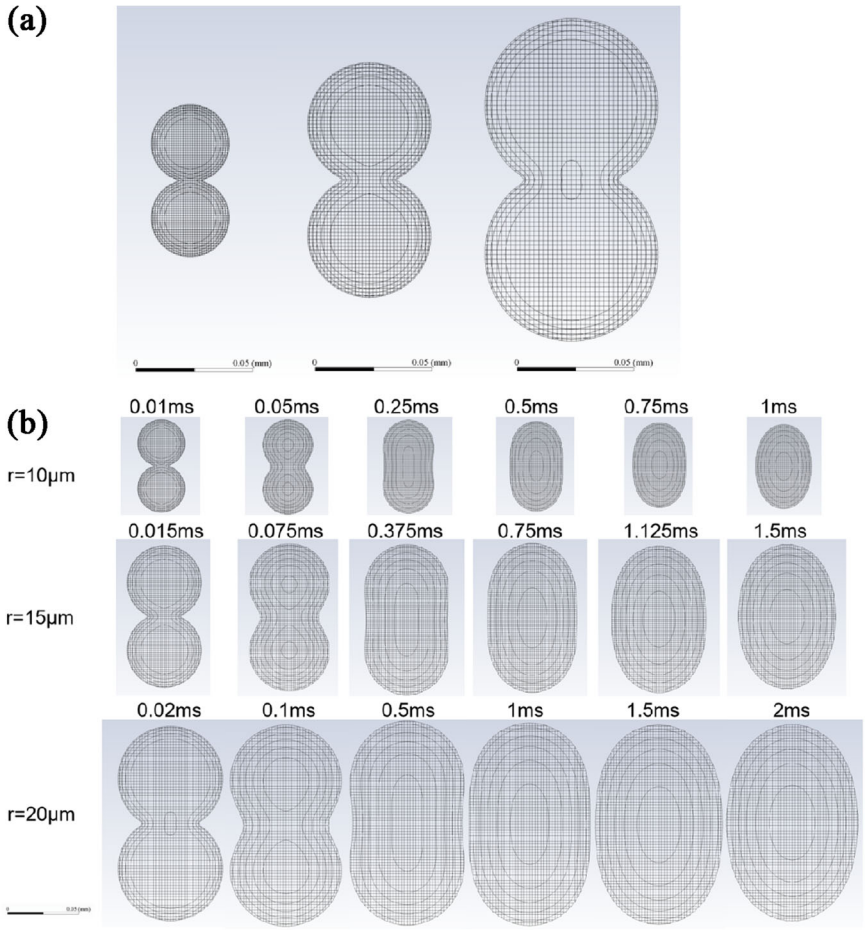

Fig. 5 Influence of droplet size in simulation. a Simulated morphology of three cases with the same measuring scale. **b** Simulated morphology of three cases at different calculation times. **a** shows the scale difference of droplets and meshes in three cases with the same measuring scale. **b** Shows the simulated morphology of these cases, but the time is chosen by the same proportion of their scale. Results verify that it takes more time for larger droplets to form a certain morphology.

the diameter of a single droplet in different cases. Because the Hoff UDF applies a greater friction effect at the contact line, the contact line moves more slowly, and the diameter is smaller than in the other two cases.

Further simulation is carried out to verify the function of the CAH UDF. The simulation comes from ref. [56], the diameter of the water droplet is 2.5 μm, the impact velocity is 0.16 m s^{-1}, θ_{adv} is 120° and θ_{rec} is 65°. Figure 3e shows the results. The left half of every image is a real photograph of the droplet. The right half shows the morphology simulated with the CAH UDF, and all results agree with the photograph better than the results in refs. [56,57], in terms of both the shapes and the dynamic contact angles, so the CAH UDF is useful to obtain a relatively accurate morphology of droplets.

Two droplets fusion simulation

Although cases without UDFs or with the CAH UDF have similar single droplet behavior, the aim of this study is to simulate the formation process of multiple deposited droplets. Some quasi-static states and contact lines moving backward will be different when using different models. The two-droplet fusion process is simulated for comparing cases without a UDF or with the CAH UDF, and the results are shown in Fig. 4a. In the early stage, contact lines move forward and mix together to form a smooth transition, and two droplets become one large elliptical droplet, and the shapes of the two cases are similar. When the velocity of the contact line is decreased as a result of viscous dissipation, the effect of applied θ_{adv} in the CAH UDF case becomes important and decelerates the moving of contact lines.

With two-droplet fusion simulations, the influence of factors can be studied. Impact velocity is difficult to measure and control in real printing processes[58], and it is related to the impact kinetic energy, so the influence of the impact velocity and the density of droplets are studied together first. The impact velocity in inkjet printing is 3–15 m s^{-1} [59,60]. Figure 4b shows the simulated results for droplets with different densities and an impact velocity of 6 m s^{-1}. No apparent differences can be found in these cases after 0.5 ms, indicating that the influence of density or impact kinetic energy mainly exists at a very early time after the droplet impacts the solid surface. This is because the volume of the droplet is tiny and the impact velocity is low, and the kinetic energy will be exhausted by viscous dissipation for a short time. Kinetic energy will not have a long-term influence. The same simulated results in the right part of Fig. 4b indicate that momentum determines the early morphology of the droplet. To summarize, the density and impact velocity of droplets have no important influence on the final simulated morphology, and they can be fixed in the following simulations.

In the single-droplet simulation, γ and η are considered together because γ/η determines the shape of the curve of the Hoffman function. In the two-droplet simulation, a series of cases with different γ and η values are simulated, and their results are classified as γ/η. Figure 4c shows the results. Cases with the same

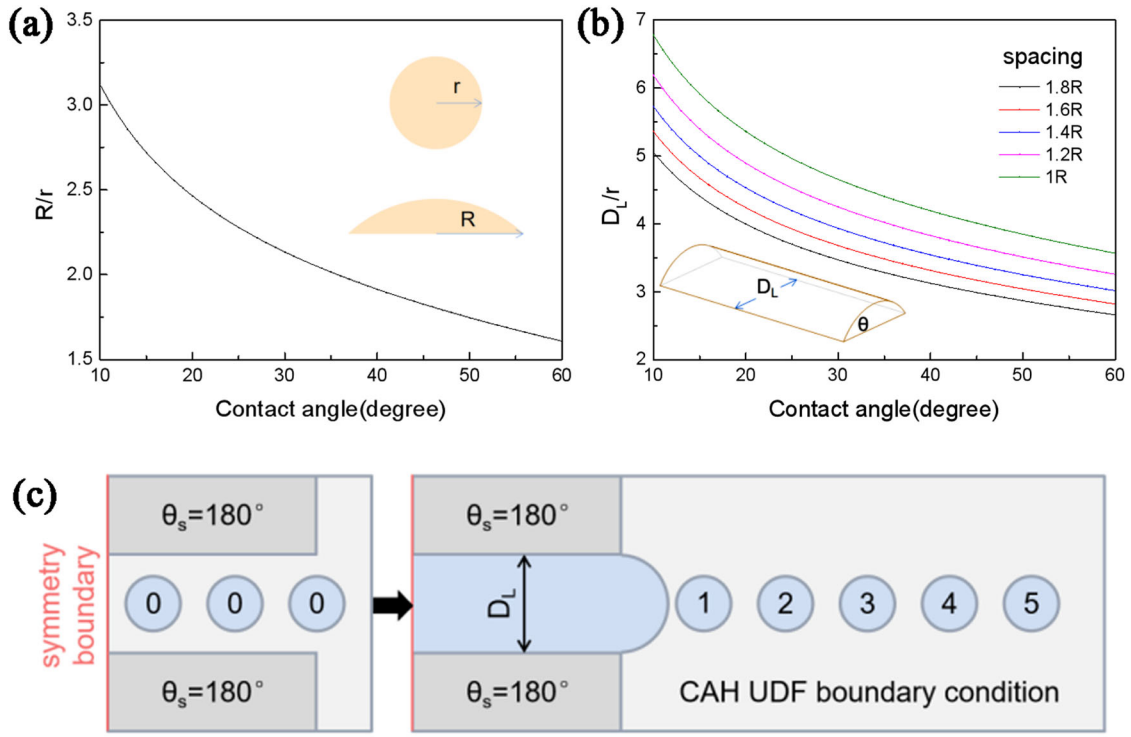

Fig. 6 Preparation of multi-droplet deposition simulation. a Scale ratio of deposited droplets to falling droplets with different static contact angles. **b** Width of a printed continuous line with different drop spacing and a static contact angle. **c** Schematic diagram of the method to avoid aggregation of droplets. In **a** *R*/*r* means the radius ratio between deposited droplets and falling droplets, and the ratio rationally decreases with increased contact angle. In **b**, D_L is the width of the printed line, *R* and *r* are the radii of deposited droplets and falling droplets, and the figure shows that both larger drop spacing and larger contact angle induce thinner lines. **c** Is the top view of the initial settings to avoid aggregation of droplets, circles with the number 0 represent initial patched droplets, and regions with $\theta_s = 180°$ are dewetting regions, the D_L is set as the value in (**b**).

values have a similar morphology, which means that the value of γ/η is also a decisive factor in the two-droplet simulation. A higher γ/η results in a faster fusion process. The fusion process of two droplets is also a moving process of contact lines and should be in accordance with the Hoffman function. It is assumed that the final static shapes of all cases are the same, so the same transition state should have the same θ_d and Ca from the Hoffman function. As $Ca = v_{contline} \cdot \eta/\gamma$, a higher γ/η requires a higher $v_{contline}$ in the same transition state. The fusion process in cases with higher γ/η values is equivalent to a film of the fusion process occurring at a higher speed.

However, real droplets are not exactly 10 μm in radius, so the scale of droplets should also be taken into consideration. Assuming that the radius of a real droplet is $f_R = 10$ μm, then the moved distance of the contact line should also be f_R times that of the simulated case. Because the dynamic contact angle corresponds to $v_{contline}$, the average $v_{contline}$ of droplets with the same γ/η and θ_s should also be the same. As a result, for the same initial and final state of the droplet, the moving time of the contact line is in direct proportion to f_R. To verify this thought, simultaneously enlarge the radius of droplets, drop spacing, the computational domain, and mesh scale in order to use the same mesh file, as Fig. 6a shows. Results are shown in Fig. 6b, in which the time is proportional to f_R, and the shape of fused droplets is almost the same in three cases except at the early time when impact kinetic energy works.

Multi-droplet deposition simulation

In multi-droplet simulations, γ/η is also regarded as a determined property of the ink fluid, and printing parameters are mainly studied in this part. The drop spacing *S* should be smaller than the diameter of a single droplet, so the scale ratio of the deposited droplet to the falling droplet (*R*/*r*) should be calculated. By equalizing the volume formula of the sphere and spherical segment, *R*/*r* can be calculated:

$$R/r = \left[4/(2/\sin\theta_s + \cot\theta_s)/(1/\sin\theta_s - \cot\theta_s)^2\right]^{1/3} \quad (11)$$

Figure 6a shows a diagram of Eq. (11). It can be observed that *R*/*r* increases with decreasing contact angle. It is assumed that the cross-section of the smooth continuous line is a circular segment, so the width of line D_L can be calculated:

$$D_L/r = 2\left[4\pi/(3\theta_s\sin^2\theta_s - \cot\theta_s)/(S/R * R/r)\right]^{1/2} \quad (12)$$

Figure 5b shows the curves of Eq. (12) with different *S* values, and a multidroplet simulation can test whether a pair of θ_s and *S* values can form a continuous line.

In the multi-droplet simulation, the aggregation of droplets at the starting point may affect the final result. To avoid this, as Fig. 6c shows, several droplets constitute the initial line, which is limited in a region with the width calculated by Eq. (12), and the left boundary is symmetric to further avoid the aggregation of droplets. Then, droplets are deposited individually after the initial line. The interval time between droplets is 0.5 ms, γ/η is 2–4, θ_s is 20–50°, and *S* decreases from 2*R* until a continuous line is generated; in this way, the maximum *S* and minimum D_L can be found.

Figure 7a shows the maximum *S*/*r* for different conditions. At a relatively low θ_s, the maximum *S*/*r* values for different γ/η values are similar, but the difference increases with the contact angle. A lower γ/η results in a larger *S* and smaller D_L, which can be explained by the relationship between γ/η and $v_{contline}$. Figure 7b

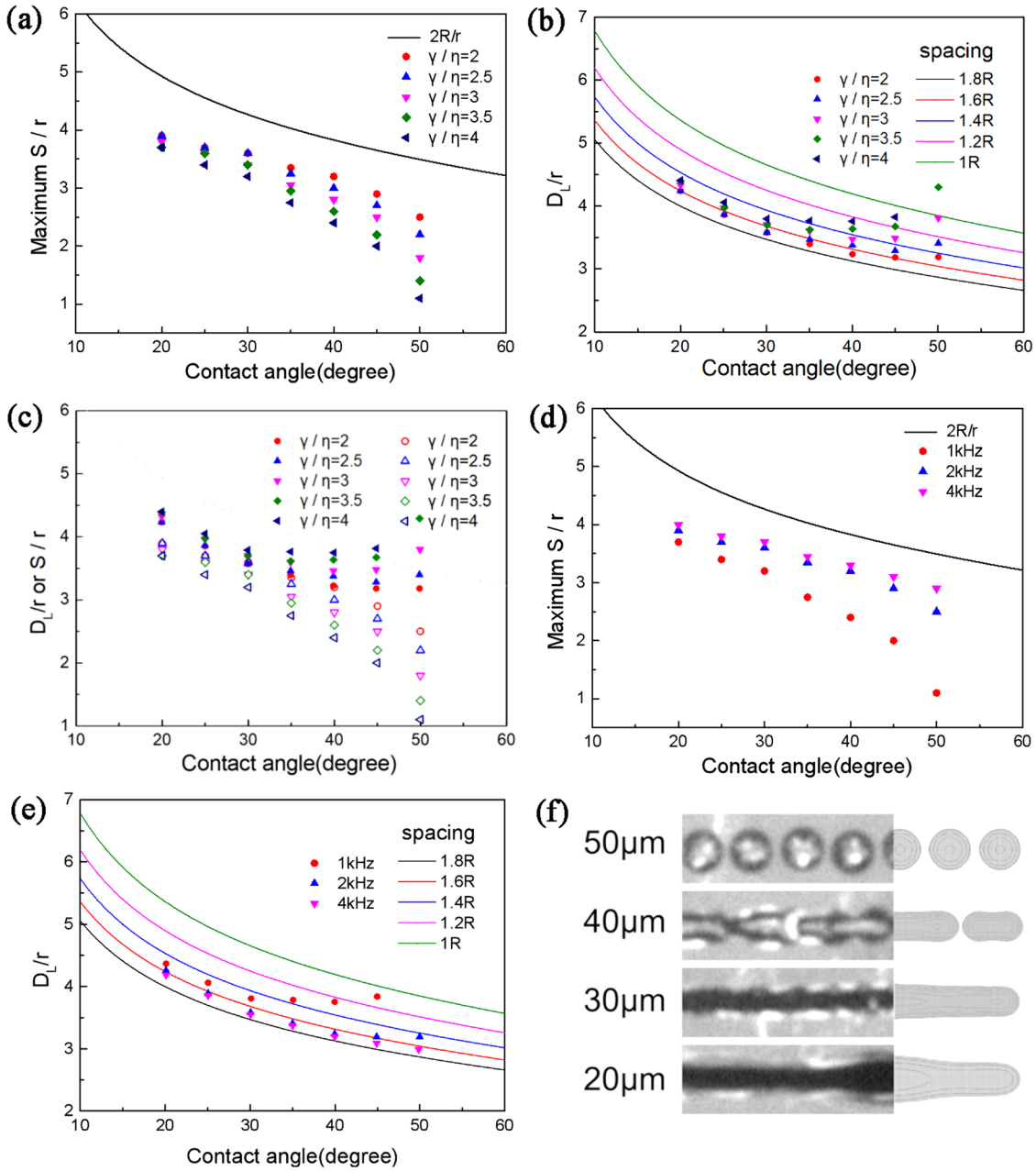

Fig. 7 Results of multi-droplet deposition simulation. a Simulated maximum drop spacing with different γ/η values. **b** Calculated minimum line width with different γ/η values. **c** Comparison of the maximum drop spacing and minimum line width. **d** Simulated maximum drop spacing with different printing frequencies. **e** Calculated minimum line width with different printing frequencies. **f** Real printed droplets and corresponding simulated results. In **a**, points represent maximum drop spacing to form continuous printed line for different conditions, and shows that small γ/η results in larger maximum spacing. **b** Shows the minimum width of lines in different conditions, this figure shows that 30–40° are proper contact angle for fabricating thinner lines. **c** Is a mixture of **a** and **b**, this figure is made to see whether the maximum spacing can be used to print sheet patterns. **d** and **e** are just like **a** and **b**, but the γ/η is fixed ($\gamma/\eta = 2$) and printing frequency is variables.

shows the minimum D_L/r of different cases. When $\theta_s < 30°$, a larger R results in a larger D_L. When $\theta_s > 40°$, droplets easily aggregate, and a smaller S is necessary to form a continuous line; thus, D_L becomes larger. Therefore, $30° < \theta_s < 40°$ is appropriate for fabricating thin single lines. Figure 7c draws the points in Fig. 7a and b together. Because the minimum D_L/r is larger than the maximum S/r, these printing parameters can be used for fabricating patterns with multirow lines.

Figure 7d and e show the simulated results of cases with $\gamma/\eta = 2$ and different f_p, and the maximum S/r increases with f_p. Because contact lines move a shorter distance during the interval time with higher f_p values, droplets have more chance to contact neighboring droplets and form continuous lines. The distinction of the results between $f_p = 2$ kHz and $f_p = 4$ kHz is not very obvious, so $f_p = 2$ kHz is sufficient for most conditions. The simulation results of cases with $\gamma/\eta = 2$ and $f_p = 1$ kHz are extremely similar to those of cases with $\gamma/\eta = 4$ and $f_p = 2$ kHz, which can be explained by the moving distance of the contact line. As discussed above, $v_{contline}$ with $\gamma/\eta = 4$ is twice that with $\gamma/\eta = 2$ at every transition state, so it takes half the time for cases with $\gamma/\eta = 4$ to obtain a similar shape. In summary, $(\gamma/\eta)/f_p$ is decisive in multi-droplets simulation, and a lower $(\gamma/\eta)/f_p$ is beneficial for improving the pattern quality. Consider the scale factor, real required f_p could be $1/f_R$ in the simulated case.

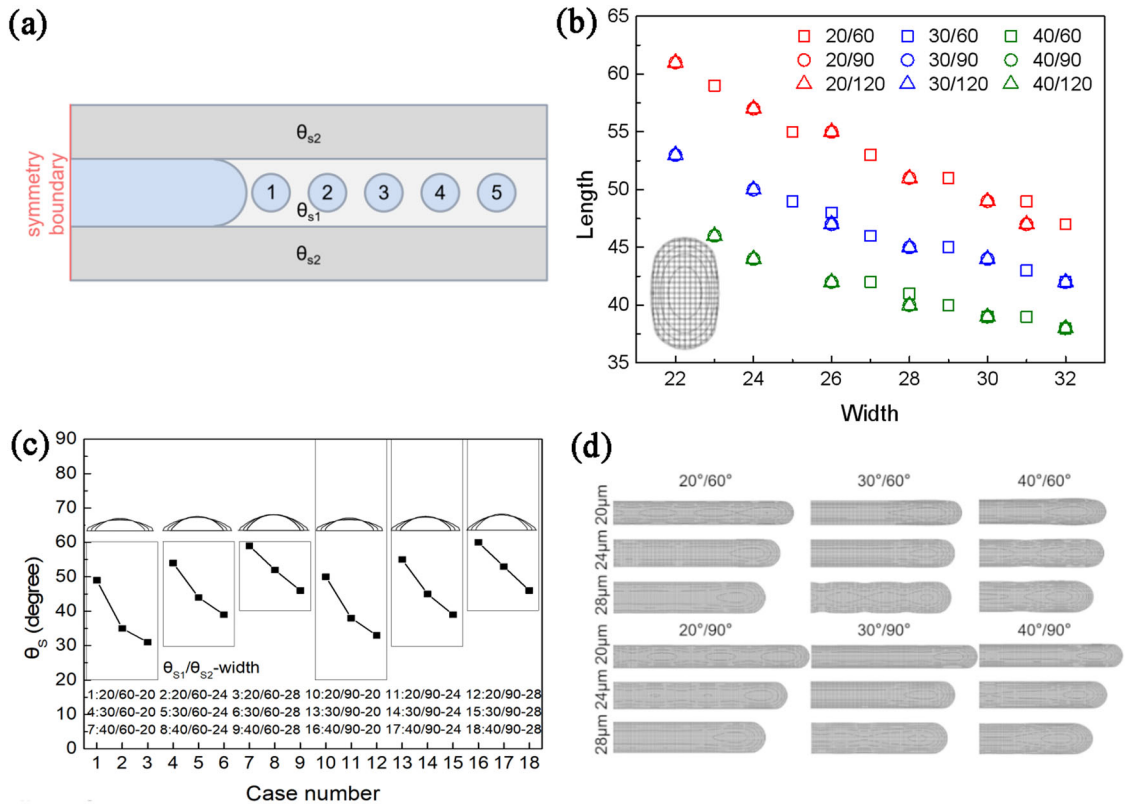

Fig. 8 Simulation of selective treatment. **a** Schematic diagram of printing with selective treatment. **b** Simulated single droplet scales of different cases. **c** Macroscopic contact angle and cross-section shape of different cases. **d** Simulated multidroplet morphology of different cases. **a** Is the top view of the computational region to realize selective treament, the contact angle of different regions are shown in the figure and droplets are deposited by the numerical order. In **b**, the number/number mean θ_{s1}/θ_{s2} and this figure shows the simulated width and length of single droplet in different selective treatment conditions. In **c**, the number/number-number of different cases mean θ_{s1}/θ_{s2}-width of θ_{s1} region, and the vertical coordinate is the macroscopic contact angle, and **d** shows the top view of simulated morphology.

To verify the simulation results, real printed lines were compared with the simulated morphology. When S decreases from 50 to 20 μm, the simulated results include isolated, scalloped, uniform and bulging formations, which are the same as the real printed formations shown in Fig. 7f.

Selective treatment on substrates is a method to improve the quality of patterns[61–63], and the effect can be simulated using models in this paper by applying different boundary conditions on different surface regions in the simulation, as shown in Fig. 8a ($\theta_{s2} > \theta_{s1}$). When $\theta_d < \theta_{s2}$, the dynamic contact angle tends to be higher and contact line tends to move backwards, as discussed. As a result, high θ_{s2} makes droplets thinner and longer.

In this simulation, θ_{s1} is 20°, 30° and 40° (CAH UDF); θ_{s2} is defined as 60°, 90° and 120° (static contact angle); the widths of the line region are 20, 22, 24, 26, and 30 μm; γ/η is 2; and the time is 2 ms. Figure 8b shows the simulated results of a single droplet. The width of the droplet decreases with the width of the line region, but the droplet is always 1–7 μm wider than the line region. The difference between θ_{s1} and θ_{s2} plays an important role in the shape of the droplet: a low θ_{s1} corresponds to an elongated droplet, while a high θ_{s2} compresses droplets into the line region. The simulation results of cases with $\theta_{s2} = 90°$ and $\theta_{s2} = 120°$ are very similar, so $\theta_{s2} = 90°$ is sufficient to have an obvious effect. Because droplets deposit on both treated and untreated regions, they are influenced by both θ_{s1} and θ_{s2} and ultimately remain in a balanced state in which the macroscopic contact angle is θ_s. Figure 8c shows θ_s and the cross-section of continuous lines, and the drop spacing is 0.9 times the length of a single droplet. The results show that θ_s is between θ_{s1} and θ_{s2}, and the height of cross-section H is relatively stable for a certain θ_{s1}; thus, θ_s decreases with increasing line region width. Moreover, both θ_s and H increase with θ_{s1}, but they are very similar for cases with different θ_{s2}, indicating that θ_{s2} has an unimportant influence. Figure 8d shows the shape of the simulated continuous line of cases with $\gamma/\eta = 2$ and $f_p = 2$ kHz, whose shapes are the same as those of cases with $\gamma/\eta = 4$ and $f_p = 1$ kHz (not shown in this paper), indicating that γ/η and f_p are not important in selective treatment assistant printing. The line with selective treatment is thin, and the edge is smooth, which is ideal for printing. However, it should be noted that the treated line region limits the movement of the contact line; for the planar treated region where contact lines move freely, γ/η and f_p also matter. In summary, selective treatment is helpful to form thinner lines and smoother edges, θ_{s1} should be lower than 30°, and θ_{s2} should be higher than 90° to obtain an obvious effect.

In summary, the friction effect plays an important role in the formation of tiny ink droplets, and the UDF proposed in this study could help to properly simulate the friction effect in Ansys Fluent. From the simulation results, the shape of the droplets is controlled by the movement of the contact line. The value of $(\gamma/\eta)/f_p$ is a decisive factor, and a small value facilitates the formation of thin lines. Overall, 30–40° is a suitable contact angle range for printing a thin single line. Selective treatment helps to print thinner lines with smoother edges. The transitional region is found for the balance of contact lines, and a higher difference is necessary to fabricate fine patterns. The inner contact angle should be lower than 30°, and the outer contact angle should be higher than 90°.

DATA AVAILABILITY

The data generated and analyzed during the study are available from the corresponding authors on a reasonable request.

CODE AVAILABILITY

The code of CAH UDF is available from the corresponding authors on a reasonable request.

Received: 2 December 2021; Accepted: 5 June 2022;
Published online: 28 July 2022

REFERENCES

1. Wong, W. S. & Salleo, A. (eds) *Flexible Electronics: Materials and Applications*. Vol. 11 (Springer Science & Business Media, 2009).
2. Gao, W. et al. Flexible electronics toward wearable sensing. *Acc. Chem. Res.* **52**, 523–533 (2019).
3. Khan, Y. et al. A new frontier of printed electronics: flexible hybrid electronics. *Adv. Mater.* **32**, 1905279 (2020).
4. Zhou, L. et al. All-organic active matrix flexible display. *Appl. Phys. Lett.* **88**, 083502 (2006).
5. Wang, W. et al. Large-scale microlens arrays on flexible substrate with improved numerical aperture for curved integral imaging 3D display. *Sci. Rep.* **10**, 1–9 (2020).
6. Bi, P. & Hao, X. Versatile ternary approach for novel organic solar cells: a review. *Sol. RRL* **3**, 1800263 (2019).
7. Yang, K. J. et al. Flexible Cu2 ZnSn (S, Se) 4 solar cells with over 10% efficiency and methods of enlarging the cell area. *Nat. Commun.* **10**, 1–10 (2019).
8. Kabachinski, J. An introduction to RFID. *Biomed. Instrum. Technol.* **39**, 131–134 (2009).
9. Lee, J. S. et al. Wireless hydrogen smart sensor based on Pt/graphene-immobilized radio-frequency identification tag. *ACS Nano* **9**, 7783–7790 (2015).
10. Baumbauer, C. L. et al. Printed, flexible, compact UHF-RFID sensor tags enabled by hybrid electronics. *Sci. Rep.* **10**, 1–12 (2020).
11. Zhang, J. et al. A review of passive RFID tag antenna-based sensors and systems for structural health monitoring applications. *Sensors* **17**, 265 (2017).
12. Wang, S. et al. Skin electronics from scalable fabrication of an intrinsically stretchable transistor array. *Nature* **555**, 83–88 (2018).
13. Heikenfeld, J. et al. Wearable sensors: modalities, challenges, and prospects. *Lab Chip* **18**, 217–248 (2018).
14. Somalu, M. R. et al. Screen-printing inks for the fabrication of solid oxide fuel cell films: a review. *Renew. Sustain. Energy Rev.* **75**, 426–439 (2017).
15. Zavanelli, N. & Yeo, W. H. Advances in screen printing of conductive nanomaterials for stretchable electronics. *ACS Omega* **6**, 9344–9351 (2021).
16. Assimonis, S. D. & Fusco, V. Polarization insensitive, wide-angle, ultra-wideband, flexible, resistively loaded, electromagnetic metamaterial absorber using conventional inkjet-printing technology. *Sci. Rep.* **9**, 1–15 (2019).
17. Sun, J. et al. A facile approach for fabricating microstructured surface based on etched template by inkjet printing technology. *Polymers* **10**, 1209 (2018).
18. Cok, R. S. et al. Inorganic light-emitting diode displays using micro-transfer printing. *J. Soc. Inf. Disp.* **25**, 589–609 (2017).
19. Zhang, L. et al. Research progress of microtransfer printing technology for flexible electronic integrated manufacturing. *Micromachines* **12**, 1358 (2021).
20. Sosada-Ludwikowska, F., Wimmer-Teubenbacher, R. & Köck, A. Transfer printing technology for fabricating chemical sensors based on tin dioxide nanowires. *Multidiscip. Digit. Publ. Inst. Proc.* **2**, No. 13 (2018).
21. Wiklund, J. et al. A review on printed electronics: fabrication methods, inks, substrates, applications and environmental impacts. *J. Manuf. Mater. Process.* **5**, 89 (2021).
22. Shams, Y. Designing a hybrid inkjet and laser manufacturing system for the digital and non-contact fabrication of emerging nanotechnology based devices. Dissertation, University of Cambridge (2019).
23. Sajedi-Moghaddam, A., Rahmanian, E. & Naseri, N. Inkjet-printing technology for supercapacitor application: current state and perspectives. *ACS Appl. Mater. Interfaces* **12**, 34487–34504 (2020).
24. Li, J. et al. Efficient inkjet printing of graphene. *Adv. Mater.* **25**, 3985–3992 (2013).
25. Liang, S. et al. *Low Temperature Interconnect Fabrication on PDMS Polymeric Substrates Using Ag Nanoparticles and Submicron Particles* 36–48 (The Japan Institute of Electronics Packaging, Japan, 2016).
26. Cai, Y. et al. Inkjet printing of particle-free silver conductive ink with low sintering temperature on flexible substrates. *Chem. Phys. Lett.* **737**, 136857 (2019).
27. Ji, H. et al. Large area infrared thermochromic VO2 nanoparticle films prepared by inkjet printing technology. *Sol. Energy Mater. Sol. Cells* **194**, 235–243 (2019).
28. Carey, T. et al. Inkjet printed circuits with 2D semiconductor inks for high-performance electronics. *Adv. Electron. Mater.* **7**, 2100112 (2021).
29. Peng, Y. et al. The elastic microstructures of inkjet printed polydimethylsiloxane as the patterned dielectric layer for pressure sensors. *Appl. Phys. Lett.* **110**, 261904 (2017).
30. Reinheimer, T., Azmi, R. & Binder, J. R. Polymerizable ceramic ink system for thin inkjet-printed dielectric layers. *ACS Appl. Mater. interfaces* **12**, 2974–2982 (2019).
31. Divvela, M. J. & Joo, Y. L. Design principles in continuous inkjet electrohydrodynamic printing from discretized modeling and image analysis. *J. Manuf. Process.* **54**, 413–419 (2020).
32. Mahajan, A., Frisbie, C. D. & Francis, L. F. Optimization of aerosol jet printing for high-resolution, high-aspect ratio silver lines. *ACS Appl. Mater. Interfaces* **5**, 4856–4864 (2013).
33. Onses, M. S. et al. Mechanisms, capabilities, and applications of high-resolution electrohydrodynamic jet printing. *Small* **11**, 4237–4266 (2015).
34. Castrejon-Pita, J. R. et al. Future, opportunities and challenges of inkjet technologies. *At. Sprays* **23**, 6 (2013).
35. Sowade, E. et al. The design challenge in printing devices and circuits: influence of the orientation of print patterns in inkjet-printed electronics. *Org. Electron.* **37**, 428–438 (2016).
36. Soltman, D. et al. Methodology for inkjet printing of partially wetting films. *Langmuir ACS J. Surf. Colloids* **26**, 15686–15693 (2010).
37. Stringer, J. & Derby, B. Limits to feature size and resolution in inkjet printing. *J. Eur. Ceram. Soc.* **29**, 913–918 (2009).
38. SarahKrainer, C. & Ulrich, H. The effect of viscosity and surface tension on inkjet printed picoliter dots. *RSC Adv.* **9**, 31708–31719 (2019).
39. Stringer, J. & Derby, B. Formation and stability of lines produced by inkjet printing. *Langmuir ACS J. Surf. Colloids* **26**, 10365–10372 (2010).
40. Lee, W. & Son, G. Numerical study of droplet impact and coalescence in a microline patterning process. *Comput. Fluids* **42**, 26–36 (2011).
41. Zhang, L., Zhu, Y. & Cheng, X. Numerical investigation of multi-droplets deposited lines morphology with a multiple-relaxation-time lattice Boltzmann model. *Chem. Eng. Sci.* **171**, 534–544 (2017).
42. Bussmann, M., Mostaghimi, J. & Chandra, S. On a threedimensional volume tracking model of droplet impact. *Phys. Fluids* **11**, 1406e17 (1999).
43. Sikalo, S., Wilhelm, H. D., Roisman, I. V., Jakirlic, S. & Tropea, C. Dynamic contact angle of spreading droplets: experiments and simulations. *Phys. Fluids* **17**, 062103 (2005).
44. Roisman, I. V. et al. Drop impact onto a dry surface: role of the dynamic contact angle. *Colloid Surf. Physicochem. Eng. Asp.* **322**, 183e91 (2008).
45. Malgarinos, I., Nikolopoulos, N., Marengo, M., Antonini, C. & Gavaises, M. VOF simulations of the contact angle dynamics during the drop spreading: standard models and a new wetting force model. *Adv. Colloid Interface Sci.* **212**, 1e20 (2014).
46. Nichita, B. A., Zun, I. & Thome, J. R. A VOF method coupled with a dynamic contact angle model for simulation of two-phase flows with partial wetting. *7th International Conference on Multiphase Flow*. ICMF 2010, Tampa, FL (2010).
47. Schmatko, T., Hervet, H. & Leger, L. Friction and slip at simple fluid-solid interfaces: the roles of the molecular shape and the solid–liquid interaction. *Phys. Rev. Lett.* **94**, 244501 (2005).
48. Gao, L. & McCarthy, T. J. Contact angle hysteresis explained. *Langmuir* **22**, 6234–6237 (2006).
49. Kistler, S. F. Hydrodynamics of wetting. *Wettability* **6**, 311–430 (1993).
50. Hoffman, R. L. A study of the advancing interface. I. Interface shape in liquid—gas systems. *J. Colloid Interface Sci.* **50**, 228–241 (1975).
51. Jiang, M., Zhou, B. & Wang, X. Comparisons and validations of contact angle models. *Int. J. Hydrog. Energy* **43**, 6364–6378 (2018).
52. Peng, X. F., Wang, X. D. & Lee, D. J. Description of dynamic contact angle on a rough solid surface. *Heat Transfer Summer Conference* **36959**, 283–288 (2003).
53. Wang, X.-D., Peng, X.-F. & Wang, B.-X. Contact angle hysteresis and hysteresis tension on rough solid surface. *Chin. J. Chem. Eng.* **12**, 615–621 (2004).
54. Cheng, K. et al. Theoretical consideration of contact angle hysteresis using surface-energy-minimization methods. *Int. J. Heat Mass Transf.* **102**, 154–161 (2016).
55. Malgarinos, I. et al. VOF simulations of the contact angle dynamics during the drop spreading: standard models and a new wetting force model. *Adv. Colloid Interface Sci.* **212**, 1–20 (2014).
56. Roisman, I. V. et al. Drop impact onto a dry surface: role of the dynamic contact angle. *Colloids Surf. A: Physicochem. Eng. Asp.* **1**, 183–191 (2008).
57. Song, Y. C., Wang, C. H. & Ning, Z. Study on spreading of liquid droplet impacting on a solid dry surface. *Appl. Mech. Mater.* **66**, 888–893 (2011).

58. Xiao, X. et al. A waveform design method for piezoelectric inkjet printhead with Doppler vibration test and numerical simulation. *Microelectron. Eng.* **196**, 13–19 (2018).
59. van der Bos, A. et al. Velocity profile inside piezoacoustic inkjet droplets in flight: comparison between experiment and numerical simulation. *Phys. Rev. Appl.* **1**, 014004 (2014).
60. Wijshoff, H. Drop dynamics in the inkjet printing process. *Curr. Opin. Colloid Interface Sci.* **36**, 20–27 (2018).
61. Yeo, L. P. et al. Selective surface modification of PET substrate for inkjet printing. *Int. J. Adv. Manuf. Technol.* **71**, 1749–1755 (2014).
62. Tang, W. et al. Controlling the surface wettability of the polymer dielectric for improved resolution of inkjet-printed electrodes and patterned channel regions in low-voltage solution-processed organic thin film transistors. *J. Mater. Chem. C* **2**, 5553–5558 (2014).
63. Nguyen, P. Q. M. et al. Patterned surface with controllable wettability for inkjet printing of flexible printed electronics. *ACS Appl. Mater. interfaces* **6**, 4011–4016 (2014).

ACKNOWLEDGEMENTS

This project was supported by the National Natural Science Foundation of China (No. 52075125).

AUTHOR CONTRIBUTIONS

S.H.: Conceptualization, methodology, writing—original draft. W.Z.: Investigation, writing—review & editing. W.Y.: Formal analysis, data curation. M.L.: Resources, supervision, funding acquisition.

COMPETING INTERESTS

The authors declare no competing interests.

ADDITIONAL INFORMATION

Correspondence and requests for materials should be addressed to Mingyu Li.

Reprints and permission information is available at http://www.nature.com/reprints

Publisher's note Springer Nature remains neutral with regard to jurisdictional claims in published maps and institutional affiliations.